applied sciences

MDPI

Article

Reliability of Thermal Conduction-Based Melt Pool Simulations Using In-Process Thermal Camera and Post-Process Single-Track Measurements

Matheus De Araujo Soares, Donatien Campion, Aurore Leclercq, Alena Kreitcberg and Vladimir Brailovski *

Department of Mechanical Engineering, École de Technologie Supérieure, Montreal, QC H3C 1K3, Canada; matheus-andre.de-araujo-soares.1@ens.etsmtl.ca (M.D.A.S.); donatien.campion.1@ens.etsmtl.ca (D.C.); aurore.leclercq.1@ens.etsmtl.ca (A.L.); alena.kreitcberg@etsmtl.ca (A.K.)
* Correspondence: vladimir.brailovski@etsmtl.ca; Tel.: +1-514-396-8594

Abstract

Laser Powder Bed Fusion (LPBF) is a complex manufacturing process that depends on precise control of printing parameters and melt pool geometry, which directly influence defect formation and final part quality. This study evaluated the reliability of a simplified thermal conduction-based melt pool model by combining post-process metallographic analysis with in situ dual-wavelength infrared thermal imaging. Experimental data were obtained through single-track printing on 316L, IN625, and CoCr alloys across a wide range of parameters. The simulated melt pool length showed strong agreement with thermal camera measurements ($R^2_{adj} > 0.78$), while the width showed moderate but consistent correlation ($R^2_{adj} > 0.52$). For melt pool depth, the model systematically deviated due to its inability to capture keyhole melting, although a strong linear correlation was still observed ($R^2_{adj} > 0.86$). Cross-validation between metallographic measurements and thermal imaging revealed only a 6–9% discrepancy, confirming the reliability of both methods and the potential of dual-wavelength cameras for industrial process monitoring. Overall, the model proves to be a reliable tool for predicting melt pool surface geometry specifically within the conduction melting regime, while its predictive capability degrades significantly in the keyhole regime, where simulated peak temperatures reach up to 7000 °C and melt pool depth errors escalate due to the disregard of recoil pressure, liquid and vapor dynamics.

Keywords: additive manufacturing; laser powder bed fusion; in situ monitoring; dual-wavelength sensor; analytical modelling; metallography measurements

Check for updates

Academic Editors: Przemysław Strzelecki, Michał Stopel, Maciej Kotyk, Joamin Gonzalez-Gutierrez and Ricardo Branco

Received: 8 May 2026
Revised: 3 June 2026
Accepted: 5 June 2026
Published: 10 June 2026

Copyright: © 2026 by the authors. Licensee MDPI, Basel, Switzerland. This article is an open access article distributed under the terms and conditions of the Creative Commons Attribution (CC BY) license.

1. Introduction

Laser powder bed fusion (LPBF) is one of the most widely used metal additive manufacturing technologies due to its ability to produce near-net-shape parts with complex shape, simplify post treatments and reduce material wastage [1]. It consists of using a laser to selectively melt a powder bed, layer by layer, according to the part geometry. However, controlling the final part quality, density, and microstructure is quite a complex undertaking [1]. Common major defects observed in LPBF parts include (a) keyhole pores, which occur because of high laser energy inputs and low scanning speeds, which in turn creates conditions for gas entrapment, and (b) lack-of-fusion defects, which occur when overlaps between neighboring laser tracks and printed layers are limited and thus leave zones of unmelted powder particles [1–3]. Both these defects are responsible for process-induced

porosity and consequently a lower mechanical resistance of printed parts [4,5]. In practice, the melt pool geometry (width, length, and depth) and temperature distribution constitute the links between process parameters and process-induced defects, and small changes in laser power, scanning speed, hatching distance and layer thickness can switch the process between the optimum and suboptimum printing regimes [1,4,5]. Moreover, these melt pool characteristics determine cooling speeds and thermal gradients accompanying the part forming process and thus affect material solidification dynamics, and therefore, the microstructure and mechanical properties of printed parts. To improve control over the process and the quality of printed parts, a plethora of in situ and ex situ monitoring methods can be used.

As far as the in situ process monitoring techniques are concerned [6–8], contact sensors such as thermocouples cannot be used directly as they would interfere with the process [8]. As such, contactless in situ monitoring methods are frequently employed. Some of them are based on the use of high-speed video cameras, which assist in observing the behavior of the melt pool and the fumes released during laser-metal interaction [6,7]. Among temperature measurement equipment, one can distinguish pyrometers which can measure the temperature within a small, defined space using point, cross, or line modes [8]. Thermal cameras, on the other hand, can measure temperatures over a larger field of view, capturing the entire extent of a melt pool, recording high-speed 2D images (typically up to tens of kHz, depending on windowing and hardware) [6,8], but they cannot be used for melt pool depth assessment. Conversely, the depth and width of a single laser track, being representative of the depth and width of a melt pool, can be measured using ex situ metallographic techniques [9–12]. Therefore, an obvious solution for measuring all the dimensions of a melt pool would involve a combination of in situ and ex situ methods [6,9,10].

Complementary to experimental techniques, simulations offer predictive links between process parameters and the melt pool geometry. Analytical or semi-analytical models based on the calculations of a thermal field created by a moving heat source provide quick estimates of the melt-pool width, length, and depth in conduction melting mode [11,12]. To be reliable, these models must be adapted to specific laser scanning and powder bed conditions, including the laser beam intensity, powder bed absorptivity, specific heat capacity and thermal conductivity [11,13–15]. For component-level planning and rapid design exploration, reduced finite element (FE) solvers, including commercial tools, offer practical setup time and cost trade-offs and can be used to predict the thermal history and distortions of a part to be printed [11]. When more detailed physics-based insights are needed, high-fidelity LPBF process models that consider the recoil pressure, the Marangoni convection, vapor dynamics, and conduction-to-keyhole transition phenomena can be used, albeit at a much higher computational cost [5].

Some studies have already analyzed the accuracy of melt pool simulations using thermal camera observations [16,17], while others have compared thermal camera observations with dimensions of solidified laser tracks obtained using conventional metallographic techniques [18,19]. However, no research has combined the use of ex situ metallographic measurements with in situ thermal camera observations to validate the results of melt pool simulations. To bridge this gap, the present study uses a combination of two experimental techniques, namely, in situ dual-wavelength infrared thermal camera observations and ex situ single-track metallography, to assess the reliability of a simplified Gaussian heat source model adapted from [12] in terms of its capacity to predict the width, length, and depth of a melt pool in LPBF. The scope of this work includes some of the most commonly used LPBF metallic materials: 316L, IN625, and CoCr alloys, shaped using variable laser powers and scanning speeds.

To the best of our knowledge, this is the first study to combine these three approaches in a single experimental campaign: analytical simulation, in situ dual-wavelength thermal imaging, and ex situ metallography. The dual-wavelength calibration approach developed here enables the emissivity-independent extraction of melt pool width, length, and temperature field directly from the thermal image, while metallography provides the complementary melt pool depth and width measurements. Altogether, these techniques deliver a complete dataset for the melt pool model assessment that covers all three melt pool dimensions plus the surface temperature field, with built-in multi-material cross-validation on the shared melt pool width measurements.

2. Materials and Methods

2.1. Melt Pool Simulations (Analytical Model)

A simplified thermal conductivity-based numerical model of the LPBF process [10,12,20] used in this work was developed in the MATLAB software (R2022b, MathWorks, Natick, MA, USA) environment. This model is used to assess melt pool dimensions and is based on analytical calculations of a temperature field generated by a moving Gaussian heat source in a semi-infinite solid (1)–(3):

$$T(x,y,z) = T_0 + \frac{AP}{kr_f\pi^{\frac{3}{2}}}\int_{+\infty}^{0}\frac{1}{1+\tau^2}exp(C)d\tau \quad (1)$$

with

$$C = -\left(\frac{\tau^2}{1+\tau^2}\right)\left(\left(\xi - \frac{Pe}{2\tau^2}\right)^2 + \eta^2\right) - \tau^2\zeta^2 \quad (2)$$

$$\xi = \sqrt{2}\frac{x}{r_f}; \eta = \sqrt{2}\frac{y}{r_f}; \zeta = \sqrt{2}\frac{z}{r_f}; Pe = \frac{r_f v}{2\sqrt{2}\alpha}; \tau = \frac{r_f}{2\sqrt{2\alpha dt}}; \alpha = \frac{k}{\rho c_p} \quad (3)$$

where T_0 is the baseplate temperature (K); A the absorptivity; P the laser power (W); k the thermal conductivity (W/(m·K)); r_f the laser beam radius (m); Pe the Peclet number; v the scanning speed (m/s); α the thermal diffusivity (m^2/s); ρ the density (kg/m^3); c_p the mass heat capacity (J/(kg·K) and dt the time (s).

The absorptivity (4) is calculated using the Hagen–Rubens model [21] approximating the material absorptivity using its electrical resistivity value:

$$A = 0.365\left(\frac{R_s}{\lambda}\right)^{0.5} \quad (4)$$

Because the raw material is in the form of a powder bed rather than a dense solid, some variables need to be corrected, namely, the density, using (5):

$$\phi = 1 - CBD \quad (5)$$

where ϕ is the fractional porosity and CBD is the coefficient of bulk powder density (without units).

The powder bed absorptivity is calculated according to [13], where the powder bed is assumed as a porous surface composed of spherical bodies and holes, all having the same temperature. Considering the bodies as "gray" without transmission of radiation, absorptivity is then equal to emissivity ($A = \epsilon$). Thus, the powder bed absorptivity can be calculated using Equations (6)–(8):

$$\epsilon_{powder} = S_h\epsilon_h + (1 - S_h)\epsilon_s \quad (6)$$

with

$$\epsilon_s = A \tag{7}$$

and

$$S_h = \frac{0.908\phi^2}{1.908\phi^2 - 2\phi + 1}; \epsilon_h = \frac{\epsilon_s\left(2 + 3.082\left(\frac{1-\phi}{\phi}\right)^2\right)}{\epsilon_s\left(1 + 3.082\left(\frac{1-\phi}{\phi}\right)^2\right) + 1} \tag{8}$$

where ϵ_{powder} is the powder emissivity (absorptivity); S_h the surface fraction occupied by pores; ϵ_h the pores emissivity; ϵ_s the emissivity of a bulk material R_s; the electrical resistivity of the material (Ω·m) and λ the laser wavelength (m).

The thermal conductivity (9) is calculated following the work of [22]:

$$k_{powder} = k_s(1-\phi)^{\frac{4}{3}} \tag{9}$$

where k_{powder} and k_s are the thermal conductivities (W/(m·K)) of a powder bed and a bulk material, respectively.

In this model, the material properties (melting temperature; material density; powder bed density; specific heat capacity; thermal conductivity and electrical resistivity) are considered constant despite the fact that, during LPBF, their values vary from those at room temperature to those near the melting point and beyond. Since it was proven in a previous work [20] that considering the material properties at 80% of the melting temperature ($0.8T_{melt}$) leads to the smallest discrepancies between calculated and measured melt pool sizes, this approach was adopted.

Using this model in the present work, in each cell of a parallelepiped domain (X = [0; 0.6], Y = [−0.25; +0.25] and Z = [−0.3; 0], all dimensions in mm, with N = 100 divisions for each axis), temperature values can be calculated. These temperatures are then compared to three material-specific threshold values: (a) vaporization temperature (T_{vap}); (b) melting temperature (T_{melt}), and (c) heat-affected zone (HAZ) temperature (T_{HAZ}), where ($T_{HAZ} < T_{melt} < T_{vap}$). This operation allows delimitation of the vaporization, melting and HAZs shown in Figure 1a, and more specifically, extraction of the melt pool dimensions (width, depth and length) shown in Figure 1b.

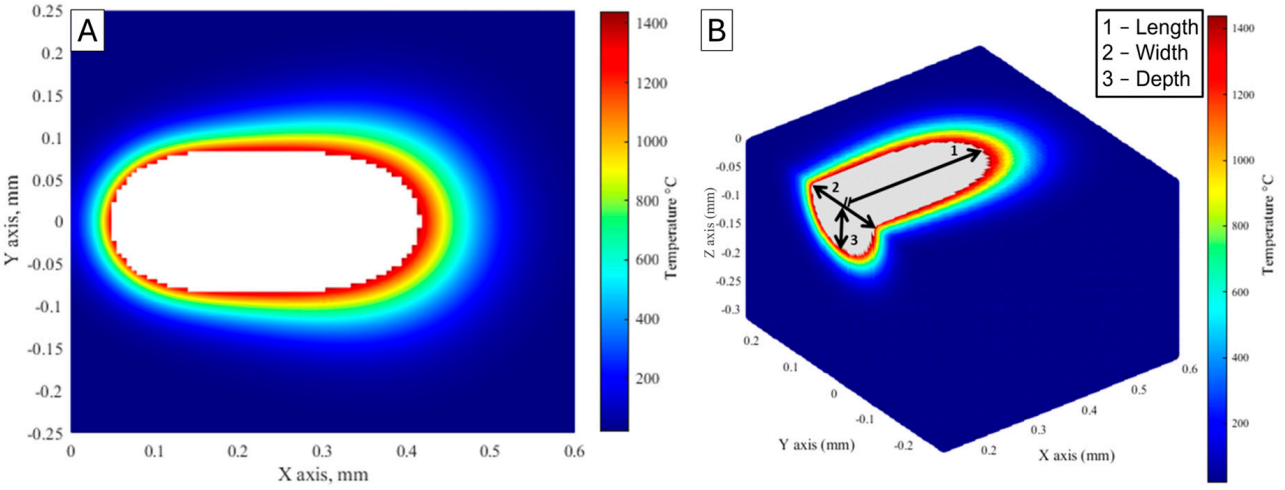


Figure 1. Simulated melt pool thermal field (316L at 215 W and 930 mm/s) showing: (**A**) different temperature zones surrounding the melt pool; (**B**) 1—width, 2—length and 3—depth of the melt pool; the temperature in the white zone is above the melting point.

To assess the reliability of numerical simulations, the melt pool width, length and depth must be experimentally measured. As was previously mentioned, no single experimental technique can provide all these dimensions at once. On the one hand, the in-process thermal camera allows the measurement of melt pool widths and lengths, and on the other, post-process single-track metallographic analysis allows melt pool depths and widths to be measured. In the framework of this study, both experimental techniques were combined to provide a complete set of experimental data (Table 1).

Table 1. Melt pool simulation and validation experiments. (✓: measured/predicted; −: not applicable).

	Melt Pool Dimensions		
	Width	**Length**	**Depth**
Simulations	✓	✓	✓
Post-process single-track metallography	✓	−	✓
In-process thermal observations	✓	✓	−

2.2. Materials

Three powder lots supplied by EOS (EOS GmbH, Munich, Germany) were used for printing: EOS Stainless Steel 316L-4441, EOS Nickel Alloy IN625 and EOS Cobalt Chrome MP1. The chemical composition and the generic particle size distributions (PSD) are given in Table 2.

Table 2. Chemical compositions (ASTM) and generic particle size distributions of three powder lots.

	Chemical COMPOSITION (wt.%)														**PSD (µm)**
Material	**Fe**	**Cr**	**Ni**	**Mo**	**Nb + Ta**	**Co**	**Mn**	**Si**	**Al**	**Ti**	**C**	**N**	**P**	**S**	
IN625	≤5.00	20.0–23.0	Balance	8.0–10.0	3.15–4.15	-	≤0.50	≤0.50	≤0.40	≤0.40	≤0.10	-	≤0.015	≤0.015	15–65
316L	Balance	17.0–19.0	13.0–15.0	2.25–3.00	-	-	-	-	-	-	≤0.03	≤0.10	-	-	20–65
CoCr	≤0.75	26.0–30.0	-	5.0–7.0	-	Balance	≤1.00	≤1.00	-	-	≤0.25	≤0.25	-	-	15–45

The material properties used for the simulations are shown in Table 3. The powder bed densities were approximated to the conditioned bulk densities (CBDs) obtained with an FT4 powder rheometer (Freeman Technology, Malvern, UK). Furthermore, for 316L and IN625, the material properties were extracted from JMatPro software (v 14.1, 2023), while for Co-Cr, they were extracted from (Carpenter Technology Corporation, Reading, PA, USA. (2020). CarTech® BioDur® CCM® Alloy—Technical Data Sheet. CRS Holdings Inc.). In all the cases, the property values correspond to ~$0.8T_{melt}$ conditions.

Although 316L, IN625, and CoCr have different thermophysical properties (e.g., thermal conductivity, absorptivity, density, and heat capacity), they exhibit relatively close melting and evaporation temperatures. This means that the phase change thresholds (solid–liquid and liquid–vapor) occur within a similar temperature range for all three materials. Since the present model does not explicitly account for phase change effects, selecting materials with comparable melting and evaporation temperatures helps minimize the influence of phase transitions on the simulation results. Consequently, differences observed between materials can primarily be attributed to variations in their thermophysical properties rather than in their phase change behavior.

Table 3. Coefficient of bulk density extracted from FT4 measurements and material properties at $0.8T_{melt}$ considered as model inputs: density, specific heat capacity and electrical resistivity are extracted from JMatPro software and Carpenter Datasheet; absorptivity is calculated using Equations (6)–(9).

Material	State of Matter	CBD	Melting Temperature (°C)	Density (kg/m^3)	Specific Heat Capacity (J/(kg·K)	Thermal Conductivity (W/(m·K))	Electrical Resistivity (nΩ·m)	Absorptivity (%)
IN625	Dense	1	1350	8440	642	27.2	130	40
	Powder	0.56		4773		13.8		53
316L	Dense	1	1400	7485	656	28.5	126	40
	Powder	0.59		4413		14.4		53
CoCr	Dense	1	1330	8407	594	32.4	99	35
	Powder	0.58		4873		15.6		50

2.3. Methods

2.3.1. Printing Experiments

Single-track printing experiments were carried out on stainless steel baseplates without preheating, using an EOS M280 LPBF system equipped with a 400 W ytterbium fiber laser (beam radius r_f = 50 µm), in an inert argon atmosphere. For each material, ten printing parameter sets (P0, P1, P2, … P9) were considered, with the laser power varying from 80 to 370 W and the scanning speed varying from 200 to 1600 mm/s, as shown in Table 4. Note that the printing parameter sets recommended by the manufacturer (optimized) are tagged as P0. To illustrate the entire printing plan for one of the three materials, 316L, all ten parameter sets are plotted in Figure 2a in the linear energy density (LED)–scanning speed (v) space coordinates.

$$LED(J/mm) = \frac{P}{v} \quad (10)$$

Table 4. Printing parameters for each of the study materials (P0 sets correspond to manufacturer's recommendations); LED is calculated using (10).

	IN625			CoCr			316L		
Parameter	Power (W)	Speed (mm/s)	LED (J/mm)	Power (W)	Speed (mm/s)	LED (J/mm)	Power (W)	Speed (mm/s)	LED (J/mm)
P0	285	960	0.30	290	950	0.30	215	930	0.23
P1	370	500	0.74	290	750	0.39	215	600	0.36
P2	285	500	0.57	350	950	0.37	335	930	0.36
P3	194	500	0.39	121	400	0.30	265	930	0.28
P4	370	960	0.39	228	750	0.30	139	600	0.23
P5	147	500	0.29	334	1100	0.30	300	1300	0.23
P6	370	1250	0.30	290	1100	0.26	370	1600	0.23
P7	80	500	0.16	200	950	0.21	154	930	0.17
P8	150	960	0.16	290	1400	0.21	215	1300	0.17
P9	200	1250	0.16	120	950	0.17	215	1600	0.13

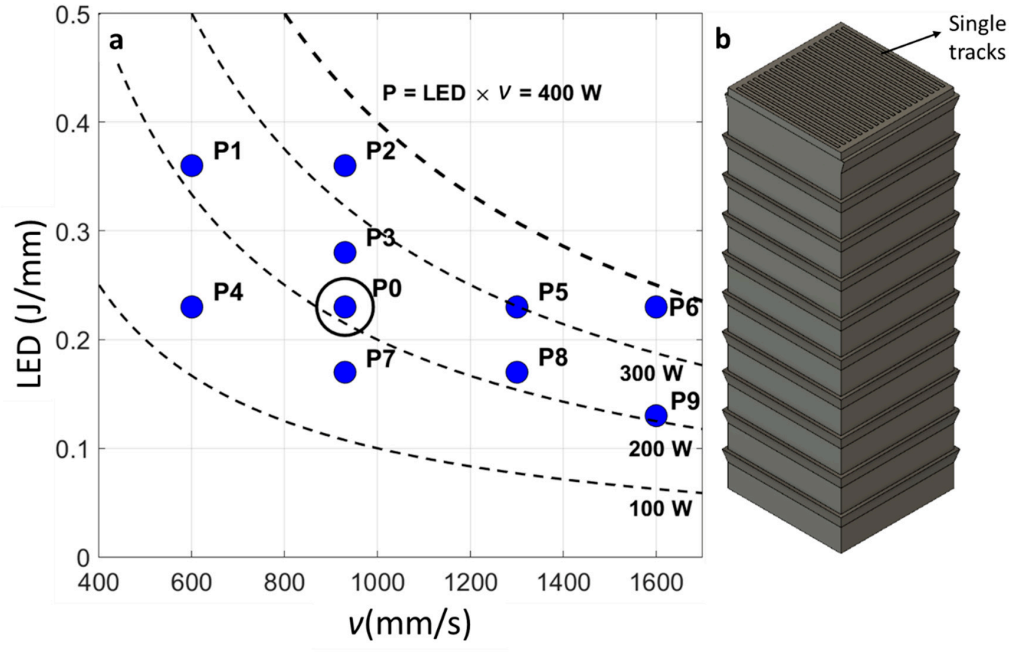


Figure 2. (**a**) Plan of experiments in the $LED - v\ space$ coordinates defined for 316L (P0 corresponds to the manufacturer-recommended process conditions); (**b**) printing strategy illustration.

Note that such a representation conveniently combines the linear energy density and scanning speed terms. The first term (LED) is commonly used in welding to control the bead geometry, while its combination with the second term (v) allows delimitation of the process window framed by the minimum and maximum powers of a laser source, since $P(W) = LED(J/mm) \cdot v(mm/s)$.

For each material, one 10 × 10 mm base prismatic specimen containing ten vertically connected zones, each 3 mm in height and with a 40 µm layer thickness, was printed, resulting in approximately 75 layers per parameter (see Figure 2b); each zone corresponded to one of the ten printing parameter sets presented in Table 4.

2.3.2. In-Process Thermal Field Measurements

To capture the thermal radiation emitted during the laser-powder interactions as part of the printing process, a dual-wavelength infrared camera (Stratonics Thermaviz, Orange County, CA, USA) was used. The system operates with 725 nm (λ1) and 900 nm (λ2) wavelength sensors, each with a 14 × 14 mm^2 (1024 × 1024 pixels) field of view and a 13.6 µm/pixel spatial resolution. The camera was aligned on-axis with the build, as shown in Figure 3. To ensure sufficient detection sensitivity for the materials and processing conditions investigated in this work, the acquisition frame rate was set between 95 and 150 frames per second (fps), while the exposure time varied between 0.01 and 0.05 ms. Neutral density filters (NDFs) with an optical density of 0.5 were used to prevent sensor saturation.

The images obtained were processed using custom MATLAB routines. First, the background noise was removed using the dark-frame subtraction method [23], followed by a manual rigid registration to minimize the displacement between each pixel across channels. For each frame, an 80 × 80 pixel region of interest (ROI) was extracted around the maximum intensity value to reduce memory usage and improve visualization (Figure 4a). Horizontal and vertical intensity profiles were also extracted across and along the lines corresponding to the maximum intensity pixels to characterize thermal gradients across and along the melt pool, respectively (Figure 4b).

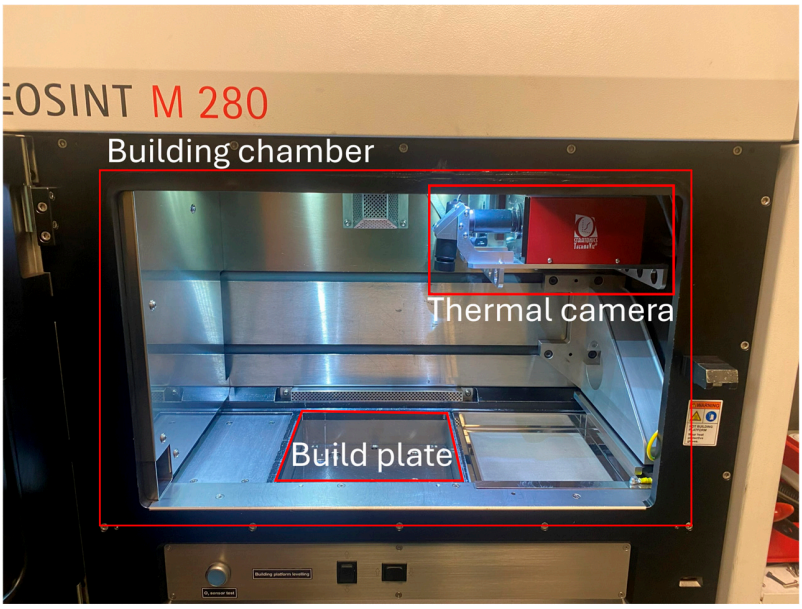


Figure 3. Equipment layout inside an EOS M280 building chamber.

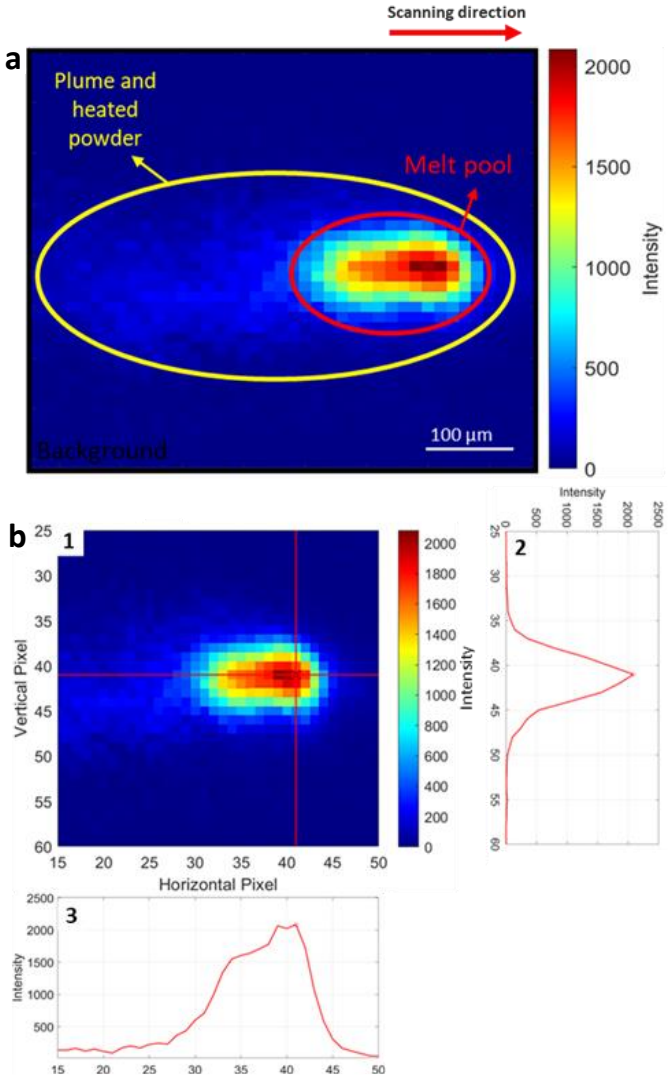


Figure 4. (**a**) Segmentation of the intensity image, (**b**) melt pool image (**1**) with corresponding intensity profiles across (**2**) and along (**3**) the melt pool; image taken from 316L-P0 using λ_1 = 725 nm sensor.

2.3.3. Conversion of Two Wavelength Intensity Values into Their Temperature Equivalents

Plotting the inverse temperature against the logarithm of the intensity ratio yields a straight line, whose slope and intercept are used as calibration constants (Figure 5). The temperature T is then given by

$$\frac{1}{T} = AlnR + B \quad (11)$$

where A and B are the constants corresponding to a linear regression [24] obtained by single-track calibration experiments on five metallic materials whose melting temperatures cover a 1500–3600 °C temperature range; R is the average intensity ratio obtained from a defined region of the powder bed. This relation allows the direct determination of the temperature value from a known intensity ratio based on the ratio pyrometry theory.

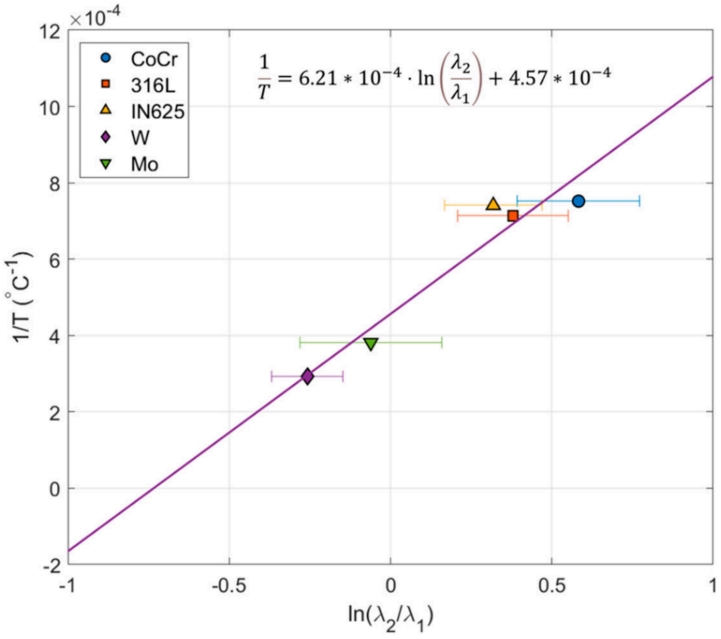


Figure 5. Calibration curve based on the melting points of a selected group of metallic materials in the 1500–3600 °C temperature range (W, Mo, CoCr, IN625, and 316L).

Note that direct pixel-by-pixel computations of the intensity ratio produce noisy temperature maps, mainly due to small misalignments between the wavelength channels, and lead to non-physical local temperature values. In this study, similar to [25], temperature isolines and particularly isotherms corresponding to the materials' melting points were used to determine the melt pool contours in each frame acquired. To this end, isolines corresponding to 90, 70, 50, 30, 10 and 5% fractions of the maximum λ_1 intensity images were defined, avoiding overlapping regions and excluding background pixels. Next, for each isoline, the corresponding pixel positions were used to sample the λ_2 image and compute the $R = \lambda_1/\lambda_2$ intensity ratio. The calibration curve was then used to convert the average intensity ratio along each isoline into an effective temperature and to plot the temperature field surrounding the melt pool.

Finally, for each temperature level, the distance from the peak intensity was computed for all the points of an isoline, and the corresponding melt pool widths and lengths were extracted. By plotting the geometric dimensions against the temperature, it was possible to identify regions associated with the vaporization, melting, and heat-affected zones (HAZs) shown in Table 5. Figure 6 contains an example of the point cloud used for the melt pool measurements applied to LPBF of 316L, where each color corresponds to one of the intensity isoline levels (5–90% of the peak λ_1 intensity).

Table 5. HAZ, melting and evaporation values for each material used (316L, IN625 and CoCr).

Material	Characteristic Temperatures (°C)		
	HAZ (0.5 T_{melt}) [26,27]	Melting (T_{melt})	Evaporation (T_{vap})
IN625	675	1350	2913
316L	700	1400	3000
CoCr	665	1330	2930

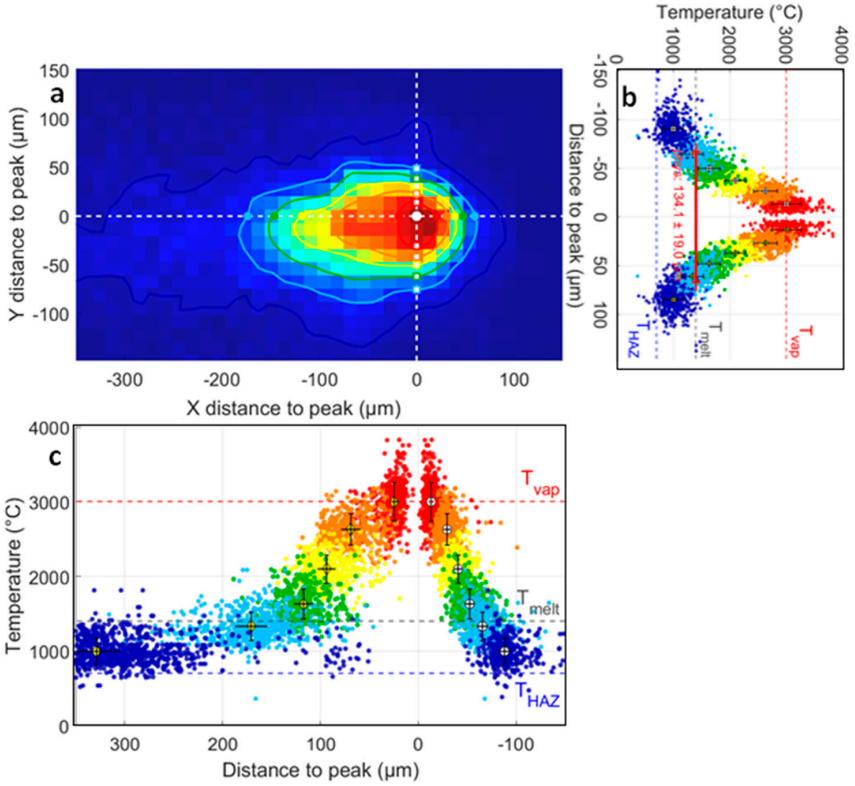


Figure 6. Melt pool image (**a**) with corresponding temperature profiles taken across (**b**) and along (**c**) the melt pool (316L-P0).

Another way of representing the camera results, which is better suited for comparison with simulations, is to plot 2D regions of interest (ROIs) associated with the vaporization (a), melting (b) and HAZ (c) temperature zones by using distances measured along and across the melt pool zone (width and length) and their corresponding threshold temperatures (Figure 7). The shaded areas represent the standard deviation of the measurements across the acquired frames.

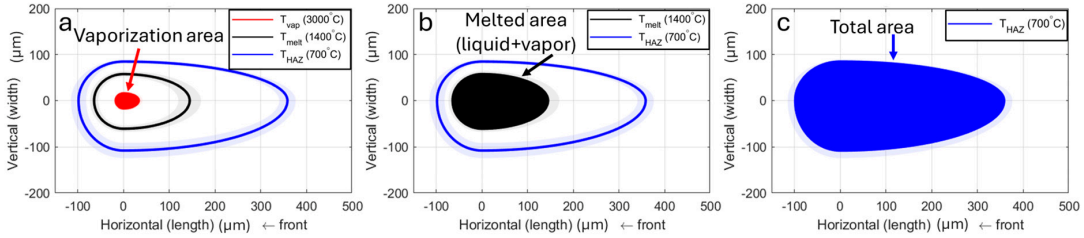


Figure 7. Representation of the camera measurements per ROI using the 316 P0 parameter set highlighting the different areas analyzed: (**a**) vaporization area; (**b**) melted area that includes the liquid and vaporization areas; (**c**) total area of a melt pool including the HAZ. Arrows indicate the scanning direction.

2.3.4. Post-Process Single-Track Measurements

After printing, a VHX 7000 Keyence optical microscope (Keyence, Osaka, Japan) having up to a 6000× magnification and a 4K resolution (4000 × 3000 px) was used for imaging and measurement. The single-track measurements (width and depth) were obtained by averaging 8 measurements from the cross-section views (Figure 8b). The melt pool characterization was defined using the top view image of the single tracks, enabling to analyze the whole track (Figure 8a). This method allows correlations to be established between in-process thermal observations and post-process metallographic measurements.

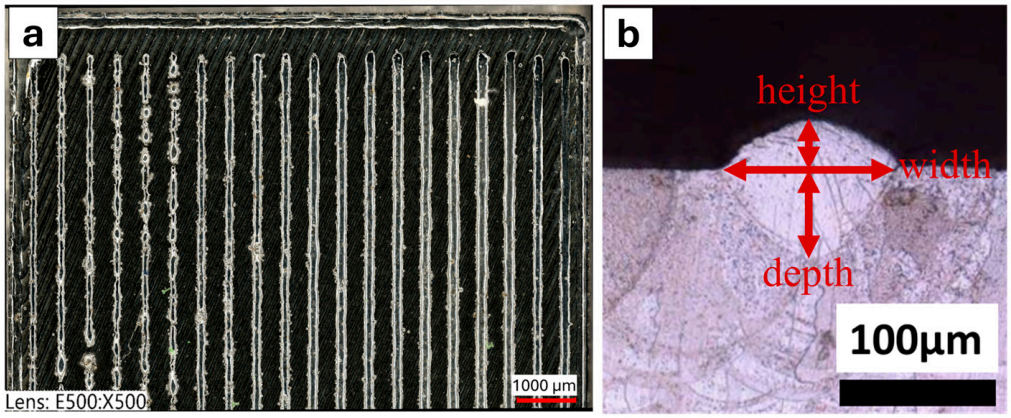


Figure 8. (**a**) Final layer with single tracks and (**b**) transverse view, highlighting measurements performed.

Measurements were performed using the image analysis software of the VHX-7000 (v. 3.0.34.332, Keyence, Osaka, Japan) provided with the microscope at 500× and 1000× magnification. The uncertainty reported in Table 6 (±5–40 µm) reflects the combined contributions of track-to-track process variability and the complexity associated with the operator-dependent identification of melt pool boundaries.

Table 6. Single-track widths and depths obtained by metallographic analyses for the three materials studied.

	IN625		316L		CoCr	
	Width, µm	**Depth, µm**	**Width, µm**	**Depth, µm**	**Width, µm**	**Depth, µm**
P0	139 ± 22	92 ± 6	134 ± 19	55 ± 9	155 ± 15	114 ± 20
P1	176 ± 17	201 ± 14	154 ± 20	110 ± 6	170 ± 22	146 ± 28
P2	166 ± 21	158 ± 16	140 ± 19	118 ± 7	166 ± 19	147 ± 26
P3	167 ± 31	118 ± 29	142 ± 19	68 ± 7	156 ± 20	64 ± 14
P4	138 ± 14	142 ± 18	129 ± 18	26 ± 6	173 ± 20	97 ± 22
P5	141 ± 15	80 ± 14	136 ± 34	52 ± 5	170 ± 22	131 ± 43
P6	128 ± 24	121 ± 14	129 ± 31	60 ± 4	167 ± 30	107 ± 36
P7	120 ± 33	11 ± 3	118 ± 29	21 ± 14	148 ± 16	57 ± 24
P8	133 ± 28	33 ± 5	124 ± 31	22 ± 8	150 ± 20	70 ± 31
P9	114 ± 27	46 ± 7	119 ± 27	18 ± 9	114 ± 28	34 ± 13

3. Results

3.1. Single-Track Measurements

Single tracks were classified using two distinct characteristics. The first classification was derived from top view observations, dividing the tracks into continuous or discontinuous (Figure 9(1A,2A,3A)). Continuous tracks (Figure 9(1A,2A)) were defined as those exhibiting an uninterrupted geometry along their length, whereas discontinuous tracks (Figure 9(3A)) presented a lack of fusion in certain sections. A second distinction was

made using the melt pool depth images (cross-section analyses), which allowed three distinct behaviors to be observed: regular, lack-of-fusion and keyhole (Figure 9(1B,2B,3B)). When the single-track depth was smaller than a one-layer thickness, it was considered to be lack-of-fusion (Figure 9(3B)); when the single-track depth was 1–2.5 times the layer thickness (Figure 9(3A)), it was considered regular, and when the single-track depth was >2.5 times the layer thickness (Figure 9(3B)), it was considered keyhole.

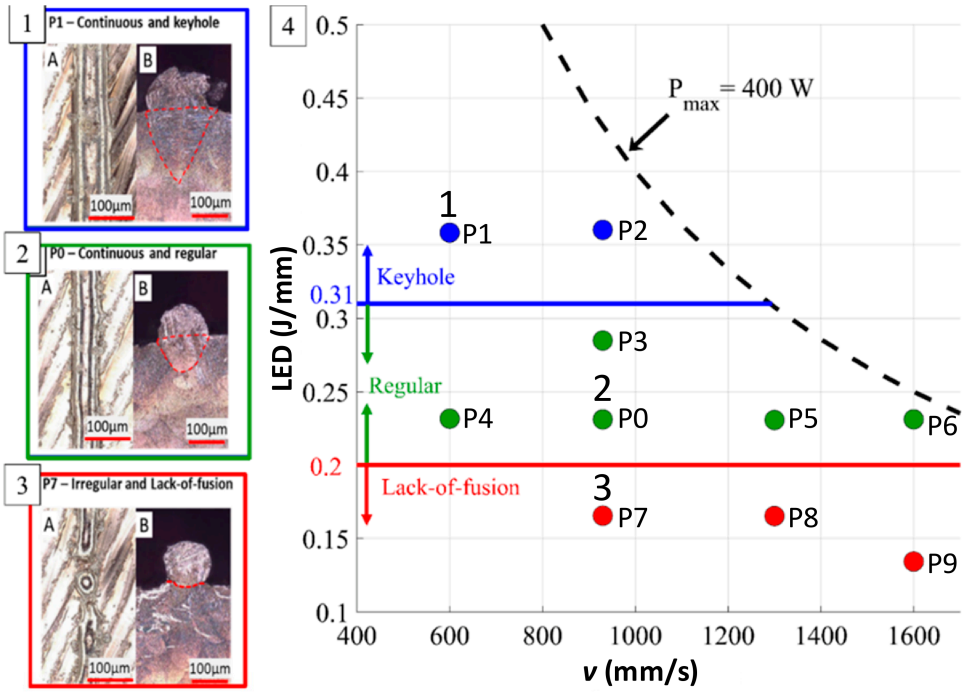


Figure 9. Single-track quality classification: (**1**) continuous and keyhole, (**2**) continuous and regular (conduction melting) and (**3**) discontinuous and lack-of-fusion using (**A**) top layer observations and (**B**) transverse views, where the red dotted line delimits the melt pool depth boundary; (**4**) single-track quality of 316L with LED levels associated with different melting regimes.

It is noteworthy that all the tracks exhibiting discontinuous geometry along their length also showed a lack of fusion in depth. Consequently, keyhole, regular, and lack-of-fusion single-track categories were retained for the remainder of the study and could be directly correlated with the linear energy density (*LED*) across all the tested materials (Figure 9(4)). Specifically, for 316L, a lack-of-fusion behavior was observed when the *LED* was below 0.20 J/mm, whereas keyhole formation occurred at *LED* values above 0.31 J/mm, leaving only regular tracks (conduction melting mode) between these two linear energy density levels, regardless of the scan speed considered. Furthermore, the measurements (Table 6) highlighted that during a constant scanning speed operation, increasing the *LED* (P7⟶P0⟶P3⟶P2) consistently resulted in increased single-track widths and depths. Conversely, for a fixed *LED*, increasing the speed (P4⟶P0⟶P5⟶P6) tended to increase the melt pool depths, but did not affect their widths.

3.2. Melt Pool Width and Length (Numerical Simulations Versus Camera Measurements)

3.2.1. Temperature Profiles

An initial comparison between simulations and experiments was carried out using melt pool width and length values obtained from the top view temperature fields predicted by numerical simulations and thermal camera observations, using the melting temperature of each material as a threshold. The point clouds corresponding to melt pool widths (Figure 10a) and lengths (Figure 10b) measured for 316L were compared with their simu-

lated equivalents (black lines in the graphs). The same procedure was executed for IN625 and CoCr (see corresponding plots in Appendix A Figures A1 and A2).

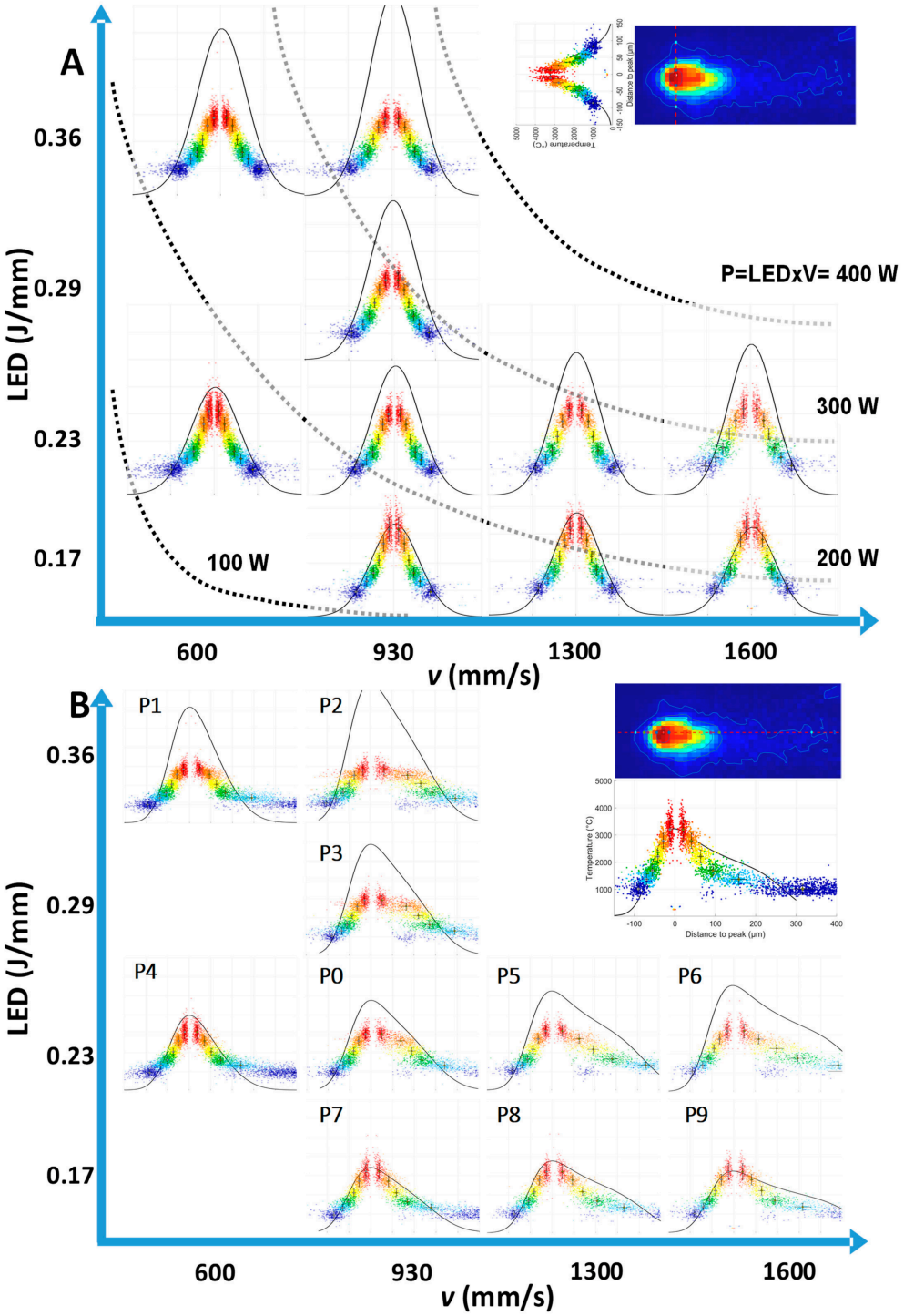


Figure 10. 316L melt pool temperature profiles obtained using simulations (black lines) and camera observations (point clouds): (**A**) width, (**B**) length.

As seen from this analysis, the higher the laser power density (P7⟶P0⟶P3⟶P2), the greater the energy input to the powder bed, the higher the maximum temperature reached, and the wider and the longer the melt pools. On the other hand, for a given *LED*, the higher the scanning speed (P4⟶P0⟶P5⟶P6), the narrower and the longer the melt pools. A clear difference between the experimental and predicted results can be seen in the maximum temperature, more specifically in the keyhole melting mode (high *LED*

values P1–P3). While the thermal camera shows a limit near the material's vaporization point (around 3000 °C), the simulations did not show an upper limit, reaching values of up to ~7000 °C, pointing to the model's limitations in terms of fairly calculating temperature distributions within the evaporation zone and in the keyhole melting mode. However, temperature distributions predicted for the melt pools produced at lower LED and v values (P4–P9) can be considered close to their experimentally measured equivalents.

The predicted melt pool dimensions were compared with the thermal camera recordings in Figure 11a,b (length and width). Relative errors were first assessed, and linear regression analyses were then performed. A simulation is considered valid when the slope (a_1) is close to 1 and the intercept (a_2) is negligible (equal to 0). The quality of the correlation is reflected by a high adjusted R^2_{adj} (as close as possible to 1) and a low RMSE, indicating good agreement between the model and the experimental data. The simulation results for the length and width, along with the corresponding relative errors, are presented in Tables A1 and A2 in Appendix A for all three materials studied.

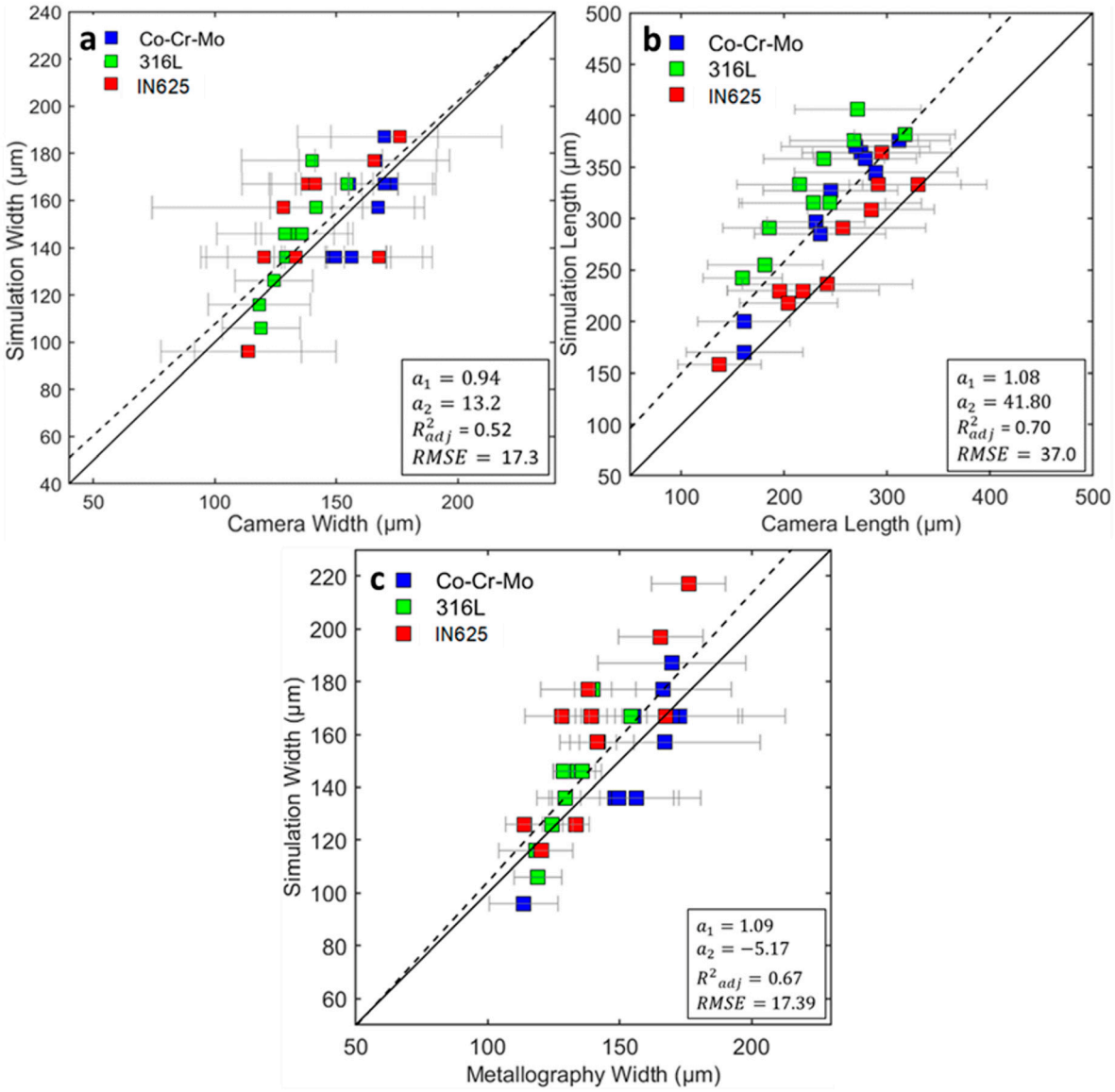


Figure 11. Simulated versus camera melt pool measurements: (**a**) width and (**b**) length for all the materials analyzed; (**c**) width compared between simulation versus metallography results. The solid line represents the perfect agreement (1:1 line), and the dashed line represents the linear regression fit.

When comparing the assessments of melt pools' widths and lengths, the simulated melt pool lengths exhibit better agreement with the experimental data than the simulated melt pool widths. For the length comparison (Figure 11b), the global linear regression yields a slope of 1.08 and an adjusted R^2_{adj} of 0.70, indicating a strong positive correlation and consistent scaling between simulated and camera measurements. The corresponding RMSE is 37 µm, reflecting the larger dimensional range involved in length measurements, corresponding to a difference of 3 pixels. For the width comparison using camera data (Figure 11a), the agreement is more moderate, with a slope of 0.94, an adjusted R^2_{adj} of 0.52, and an RMSE of 17.3 µm. Although the linear trend remains evident, the scatter in width measurements is larger than that in length measurements.

To further validate the in situ monitoring approach, simulation measurements are compared with post-process metallography in Figure 11c. The resulting regression shows a slope of 1.09 and an adjusted R^2_{adj} of 0.67, with an RMSE of 17.39 µm. The slope slightly above unity suggests a tendency for the simulated measurements to overestimate their metallography-obtained equivalents, with this discrepancy remaining limited. Overall, these results confirm that the simulations provide reliable predictions of the melt pool dimensions, capturing the correct trends while maintaining dimensional errors within an acceptable range.

3.2.2. Melt Pool Area

The 2D thermal camera maps are plotted in the $LED - v$ *space* in Figure 12a for 316L to illustrate how the thermal zones evolve in these coordinates. It can be observed that the melted zone increases with an increase in the *LED* (P7⟶P0⟶P3⟶P2) and scanning speed values (P4⟶P0⟶P5⟶P6). Conversely, no clear trend can be observed in the evolution of the vaporization and HAZs with respect to process parameters. The simulated thermal fields presented in Figure 12b show similar trends when compared to their thermal camera equivalents as far as the melting zones are concerned. An increase in both the energy density and scanning speed produces larger melting zones. However, contrary to the thermal camera observations, simulations also reveal HAZ-related trends, with an increased HAZ corresponding to higher energy inputs.

Two main discrepancies between the simulations and the camera observations must be highlighted, the first related to the vaporization zone, and the second, to the HAZ. In both zones, results obtained with the thermal camera cannot be reliably used, for reasons related to the sensor temperature calibration range, which in this study corresponds to 1000–3000 °C. Since both the temperature above vaporization and HAZ temperatures fall outside this range, thermal camera measurements in these zones become irrelevant. Nevertheless, the simulated and thermal camera-observed melting zones follow the same trends and can therefore be compared, even though the camera's melt pools manifest a tear-drop shape, while the simulated melt pools are more ellipse-like. It can be inferred that the ellipse-like shape of the melt pool in simulations is due to a simplified Gaussian beam heat source model.

Finally, it can be observed that the higher the laser power, the larger the melt pool areas obtained from simulations (Figure 13a) and observations (Figure 13b). For 316L, the simulated melted area varies from 0.021 to 0.058 mm^2, while the total area goes up to 0.085 mm^2. The camera results show a similar trend, although with smaller melted areas in the 0.017 to 0.041 mm^2 range. It can therefore be concluded that simulations overestimate the melt pool dimensions as compared to thermal camera observations. These discrepancies hold for all three materials studied and can be explained by two factors: first, the calculated temperature profiles reach unrealistic peaks, greatly exceeding the boiling point of the material (up to 7000 °C) and thus expanding the calculated high-temperature

zones. Second, the camera readings are capped by the sensor calibration range and therefore by temperatures approaching the material vaporization temperatures, thus reducing the size of the experimentally observed high temperature zones.

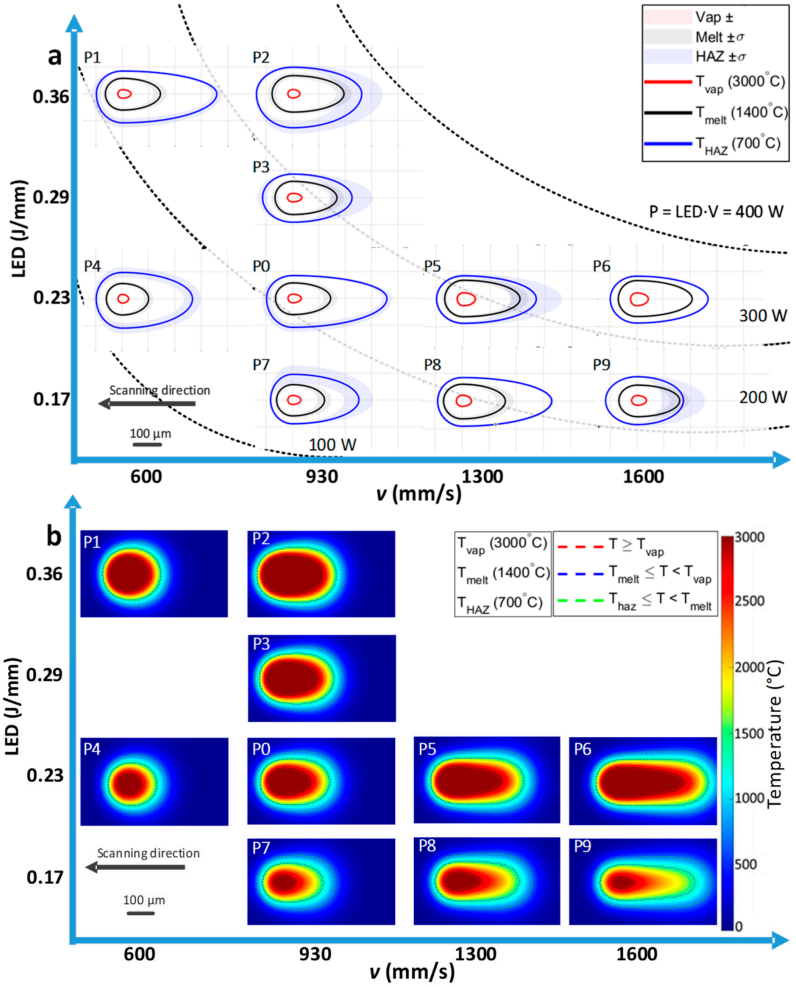


Figure 12. (**a**) Averaged 2D thermal maps obtained using thermal camera for 316L; (**b**) simulated thermal maps for 316L, the color scale is limited to 3000 °C.

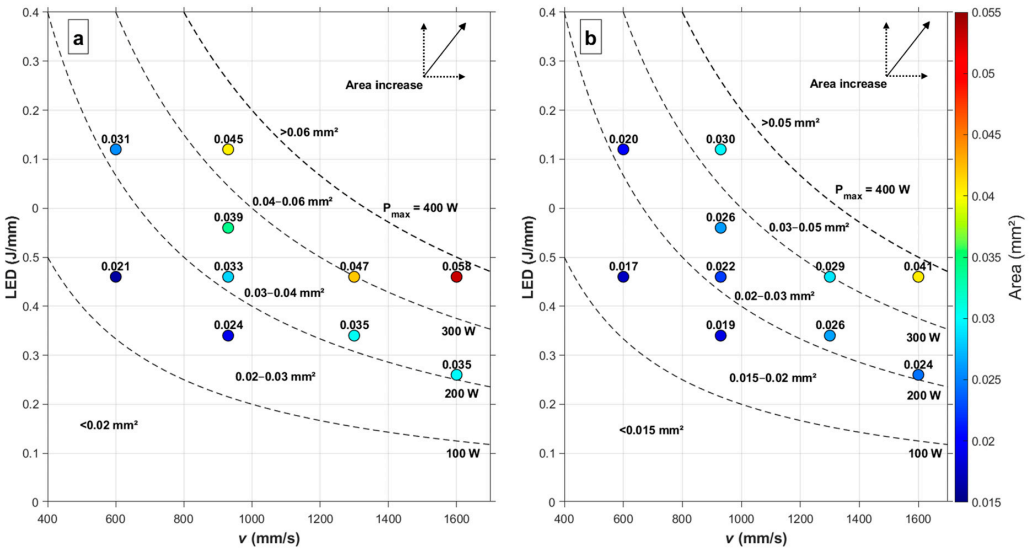


Figure 13. Melt pool area for 316L: (**a**) simulations, (**b**) thermal camera observations.

When area data for all three materials are grouped together (Figure 14), the linear fit yields a_1 = 1.30, with an adjusted R^2_{adj} of ~0.80 and an RMSE of 0.005 mm^2. This indicates that, overall, the model overestimates the melt pool area by approximately 30% as compared to camera observations, while still preserving a good correlation.

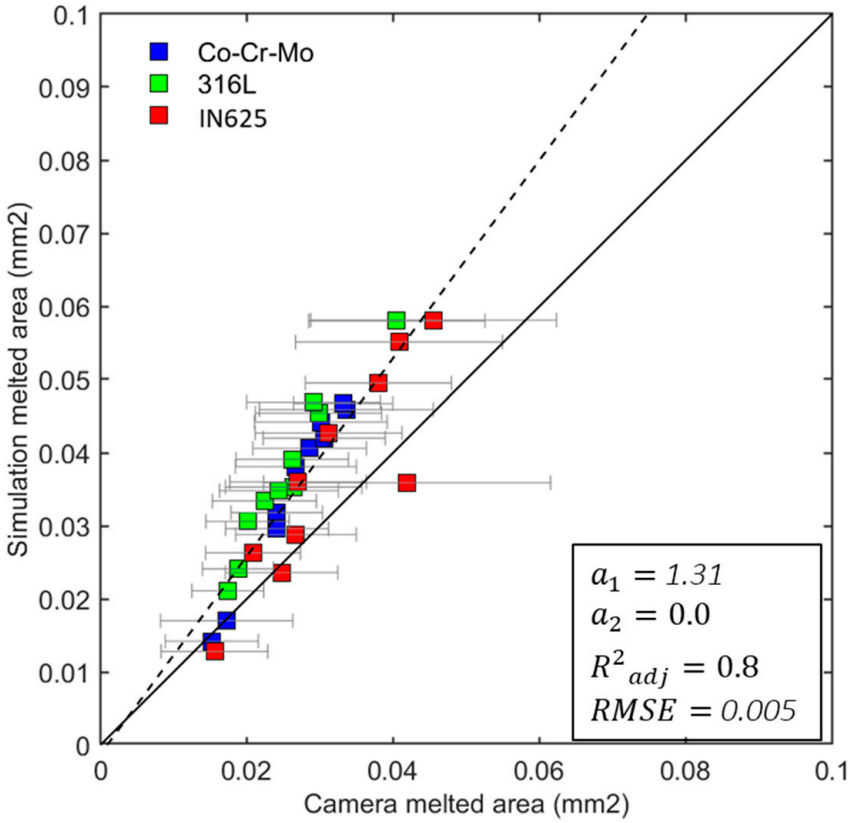


Figure 14. Melt pool area: simulations versus camera measurements. The solid line represents the perfect agreement (a_1 = 1), and the dashed line represents the linear regression fit.

3.3. Melt Pool Depth (Simulations Versus Metallography)

Comparing the calculated melt pool data with their metallographic equivalents (Figure 15) enables assessing the limitations of a heat conduction-based model regarding the melt pool depth calculations. It can be noted that the closest proximity between both sets of data (discrepancy under ±20%) corresponds to the melt pool depth values ranging from 35 to 100 µm (1–2.5 times the layer thickness), i.e., to the occurrence of regular tracks in conduction melting mode. In the keyhole melting region, where the energy input is higher, the greater the melt pool depth, the greater the discrepancy between simulations and experiments, with the discrepancy reaching values as high as 100%. When lack-of-fusion defects occur, the voids (pores) in the solidified substrate act as thermal insulators (heat transfer is much slower than in fully dense solid), a fact not taken into account in the model (this region is named LOF in Figure 15). For measured depths between 10 and 35 µm, the model overestimates the experiments, with a difference of ~30%, while following linear regression with a low dispersion (R^2_{adj} = 0.84), which is an excellent fit. The measurements and relative errors for all the materials are presented in Table A3 in Appendix A.

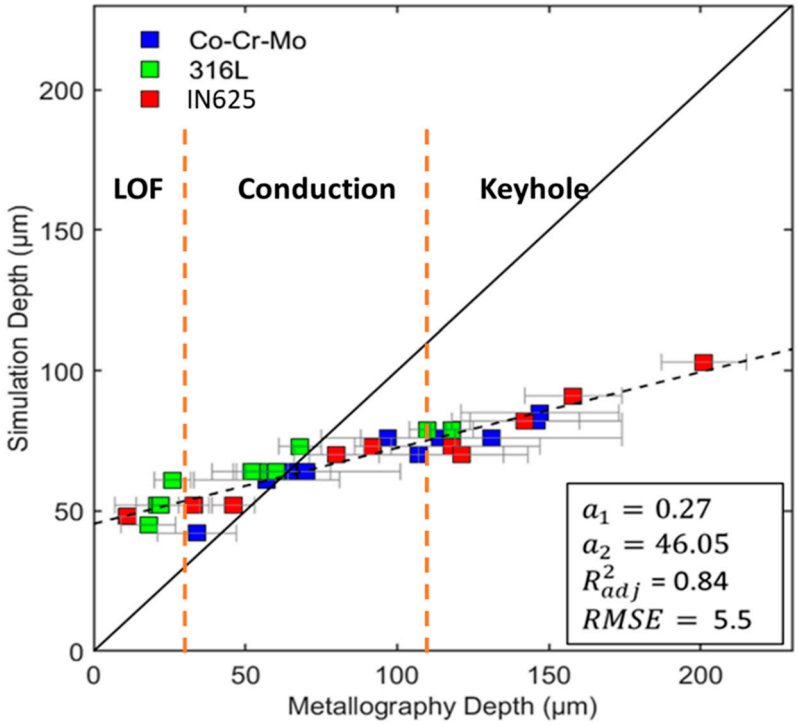


Figure 15. Melt pool depth: simulations versus metallography results. The solid line represents the perfect agreement ($a_1 = 1$), and the dashed line represents the linear regression fit.

4. Discussion

The commercial calibration method for a dual-wavelength thermal camera, which consists of resistance-heating a tungsten filament [28], could not be used in this work. This procedure led to maximum temperature readings exceeding 5000 °C, which is more than 1000 °C above the vaporization point, which is not physically relevant. Furthermore, the background temperature readings were higher than the melting point of the materials analyzed, making it impossible to define the melt pool boundaries. Additionally, the temperatures at the border of melt pools were above 3000 °C, which also did not correspond to the expected temperatures. In contrast, the new calibration method used in the present study brought the overestimation of the boiling point to only ~100 °C, representing an 80% reduction. This approach also allowed us to directly apply the melting temperature threshold to measure the melt pool dimensions.

Significant differences between the vaporization temperatures and the maximum temperatures obtained with thermal cameras have already been observed in the literature [29–31], with overestimations varying from ~300 °C to ~500 °C, and being limited by a saturation of sensors. These discrepancies have often been attributed to plume formation or the presence of metal vapor in the optical path between the camera and the melt pool, which interfered with intensity readings. Studies [30] have also reported difficulties in reaching the melt pool values.

The calibration curve of the present work was obtained by correlating the results of post-process melt pool metallographic analyses with thermal measurements, and the procedure used is explained in more detail in [32]. Although this type of calibration has not previously been reported for dual-wavelength thermal cameras, a similar approach was adopted for a high-speed infrared camera in [19]. Some equipment producers also suggest applying a constant emissivity across the melt pool, using a single emissivity value calculated at a specific point or region, and generalizing for the whole image. In this study, the pixel-by-pixel ratio was calculated in different regions of the thermal image, thus

minimizing the dependence on emissivity. Finally, it should be noted that the calibration developed in this work was performed for a single neutral-density filter configuration. Therefore, the resulting relation between the intensity ratio and the temperature was validated only for this optical setup.

Temperature measurements using dual-wavelength infrared cameras carry significant limitations, the first being the spatial resolution. In the setup used in this work, the pixel size is 13.6 μm in the plane measured, which defines the spatial image resolution. For the melt pool widths in the 100–200 μm range, this means that a one-pixel difference in measurements would correspond to roughly 7–14% melt pool width variations. Consequently, even small uncertainties in the edge detection or the threshold value can translate into relatively large errors, especially for smaller melt pools [18]. Another limitation of the thermal measurement method developed in this study is the presence of a quite narrow 1000–3000 °C calibration range, also reported in [17]. The upper bound prevents an adequate delimitation of the vaporization zone, while the lower bound does not allow adequate definition of the HAZ.

A high-speed CMOS thermal camera has already been used to measure the melt pool width of 316L, with the laser power varied from 100 to 600 W, and the scanning speed, from 400 to 1100 mm/s [18]. In that work, the melt pool contour was determined using a light intensity threshold and a Sobel edge detection filter. The difference between camera and metallographic measurements ranged from −54 to 36% with an average relative error of ~3%. Similar trends were observed in the present work with a ~5% discrepancy for 316L and 7% discrepancy for all three materials. Overall, notwithstanding these limitations, using the thermal camera to validate melt pool measurements and temperature profiles proved to be suitable, especially when it came to comparing values of the melt pool lengths and areas.

The results provided by our simulations can be clustered into two groups, the first being the overall temperature distributions and the peak temperatures, and the other, the proximity of the melt pool width, length, depth and surface area values obtained by simulations to those obtained experimentally.

For the temperature profiles obtained, it was verified that an increase in the *LED* values also increased the maximum temperature in the melt pool, which was expected, since the energy input also increased. However, it was seen that the maximum simulation temperature was much higher than the vaporization points of the materials, going up to a maximum of 7000 °C, which had also been observed in similar melt pool simulation-related studies [33]. These discrepancies are related to the models' simplifications, such as neglecting multiple physical phenomena related to the process, including the Marangoni effect, the recoil pressure, the different heat transfer modes and the solid–liquid–vapor phase transformations [34]. These simplifications allowed us to significantly decrease the computational time but at the expense of a reduced model fidelity. For example, when the vaporization effect was considered in [35], the maximum temperature calculated in the Ti-6Al-4V alloy's melt pool was reduced by ~50%, going from 6000 to 3050 °C, and the melt pool width measurement error was reduced from ~60 to ~3%, which led to a 30% reduction in discrepancy between the simulated and camera-measured melt pool area values.

The applicability of the present model is therefore reliable in the conduction melting regime, defined here by the linear energy density ranges 0.20 < LED < 0.31 J/mm for 316L, 0.21 < LED < 0.39 J/mm for IN625, and 0.21 < LED < 0.37 J/mm for CoCr. Within this window, melt pool surface dimensions (width, length, and area) and peak temperatures, in some cases, can be predicted with confidence. In either the keyhole regime or the lack-of-fusion regime, the model proved to be a useful tool for trend analysis rather than for exact predictions. Accurate prediction of melt pool depth and peak temperature in these

regimes would require the inclusion of recoil pressure, liquid and vapor dynamics, which are beyond the scope of the simplified formulation used here.

The simulations systematically overestimate the melt pool area by ~30%, which can be attributed to two contributions of comparable magnitude. First, the analytical model of this study disregards the liquid and vapor dynamics involved in melt pool formation, including energy losses from the melt pool surface due to evaporation and the downward recoil pressure that redistributes heat into the depth direction. In this context, Karayagiz et al. (2019) [35] demonstrated that the explicit accounting for vaporization in LPBF Ti-6Al-4V reduces the peak temperatures by ~50% and decreases the melt pool width calculation errors from ~60% to ~3%, suggesting that vaporization is responsible for most of the surface-area overestimation. Second, the thermal camera's upper calibration limit at 3400 °C restricts the measurable temperature range. Above this threshold, the temperature mapping becomes unreliable, preventing accurate quantification of the vaporization zone. However, the rest of the temperature field, including the melting isotherm used for melt pool boundary extraction, remains within the calibrated range and is therefore unaffected. A more rigorous treatment of both effects would require either extending the camera calibration validity above 3400 °C or incorporating a vaporization-limited temperature cap in the simulation framework. Both approaches are recommended for future work.

The morphological validation we performed showed that the strongest correlation between the model and experimental measurements was achieved for the total melted area, with R^2_{adj} values ranging from 0.8 to 0.93. Among the alloys studied, CoCr exhibited the best predictive performance in general for all the melt pool geometrical metrics considered. This behavior is likely associated with the fact that, under the investigated process conditions, CoCr tends to operate closer to a conduction-dominated regime, where heat transport is mainly governed by diffusion and assumptions of the simplified thermal model remain closer to reality than for the two other metallic alloys, i.e., 316L and IN625 [36].

At the same time, the linear regression coefficient (a_1) ranged mostly between 1.0 and 1.5 and the $a_2 > 0$, meaning that there was a 30% systematic overestimation for all the materials. These results align with the findings in [37], which also revealed a significant overestimation of the simulation data as compared to experiments, especially at higher laser powers, where the model did not consider variations in the laser absorption values.

Regarding the melt pool length, the model showed the highest predictive performance, with an R^2_{adj} of 0.97 for CoCr. The simplified model also properly represented the effects of printing parameters, especially the scanning speed, on the melt pool tail. Between the three dimensions measured (width, length and depth), the length was shown to be the least sensitive to approximations of the simulation model of this study.

In contrast, the melt pool width exhibited a higher sensitivity and greater dispersion, with a_1 varying from 0.85 to 1.7. This increased variability can be associated with the fact that alloys such as IN625 and 316L are more susceptible to transition toward fluid-driven regimes, where melt pool convection and recoil pressure effects become more relevant, reducing the predictive accuracy of thermal conduction-based models [36]. However, the same trend as above was also respected, with the width increasing with an increase in the laser energy density, as was also observed by other authors [38,39].

Furthermore, 316L presents a combination of a relatively high melting temperature, elevated absorptivity, and moderate thermal conductivity that makes its melt pool more sensitive to convective flow and stochastic variations. As a result, localized keyhole formation may occur at higher laser energy densities, producing narrow and deeper melt pools and reducing peak temperatures as compared to model predictions [36,40].

These observations naturally demonstrate that conduction-only models are more reliable for alloys and conditions in which heat transport remains predominantly in conductive mode and melt pool dynamics are moderate. In alloys like 316L at higher laser energy densities, where convective transport and localized keyhole effects become more significant, deviations from conduction-based predictions are expected [41]. This notwithstanding, simplified thermal-conduction models remain a valuable tool for rapid first-order simulations and process parameter exploration.

Despite a relatively good correlation between melt pool surface measurements (width, length and area), the predicted melt pool depth presented significant agreement with the metallographic results only within the conduction melting mode. As shown in Figure 15, a linear regression coefficient of ~0.3 confirms that a thermal conduction-based model is clearly unsuitable for melt pool depth prediction in the case of large pores in a solidified substrate and keyhole melting, since the model does not consider the reduced effective conductivity in porous regions. The same was also reported in [42,43], where a simplified simulation model predicted the width correctly, but underestimated the depth outside the stable conduction melting mode. Regarding the high energy inputs ($LED > 0.3$ J/mm), any simulations that neglect the vapor and recoil pressure phenomena, which are responsible for a higher downward heat transport [44,45], underestimate the melt pool depths. Conversely, for irregular tracks with low energy inputs ($LED < 0.2$ J/mm), simulations overestimate the melt pool depth, since the model assumes continuous melting and does not consider cooling and incomplete powder sintering [45].

Given the strong linearity observed ($R^2_{adj} \geq 0.86$) and the regression slope of approximately 0.3 in the keyhole regime, an empirical correction can be implemented by multiplying the simulated depth slope by a compensation factor of $k_d \approx 1/0.3 \approx 3.3$ (based on Table 7). This correction would enable the conduction-based model to serve as a rapid predictive tool across the entire process window, including the keyhole regime, albeit with reduced physical fidelity. For physically reliable predictions in the keyhole regime, the model should be extended to incorporate the previously discussed physical phenomena, including recoil pressure, liquid Marangoni convection, and vapor dynamics. Further validation of this compensation strategy across additional materials and process conditions is recommended for future work.

Table 7. Results of linear regression analyses between the experiments and simulations of the melt pool length, width, depth, and the melted area for all three materials.

	IN625				316L				CoCr			
	a_1	a_2	R^2_{adj}	RMSE	a_1	a_2	R^2_{adj}	RMSE	a_1	a_2	R^2_{adj}	RMSE
Length	1.1	7.6	0.88	20	1.0	90	0.78	22	1.4	27	0.97	18
Width	0.85	34	0.43	19	1.7	−90	0.76	9.63	1.4	−63	0.80	11
Depth	0.29	42	0.94	4	0.3	47	0.86	3.8	0.3	41	0.86	4
Melted Area	1.2	0.0	0.8	0.01	1.5	0.0	0.93	0.003	1.4	0.0	0.9	0.003

5. Conclusions

The present study performed a reliability assessment of the simplified Gaussian heat source thermal conductivity-based melt pool LPBF model for 316L, IN625, and CoCr alloys using a combination of the in-process thermal camera and post-process single-track measurements; the main results demonstrated the following:

- The model accurately predicted the melt pool geometry features (width, length, and melted area) across a wide range of process parameters corresponding to the con-

duction melting mode. The melt pool length showed the highest agreement with the thermal camera measurements ($R^2_{adj} > 0.78$). The prediction of a melt pool width showed a more moderate agreement due to its inherent sensitivity to the Marangoni effect; however, the overall trends remained compatible with experimental observations and confirmed that thermal conduction-based models are highly effective for predicting the melt pool surface geometry in the conduction melting regime.

- Quantitative prediction of the melt pool depth was found to be limited outside the conduction melting regime, with a regression slope of approximately 0.3 observed. This underestimation in the high-energy regimes and overestimation in the lack-of-fusion zones reflect the main limitations of the model in terms of its capacity to simulate the keyhole dynamics and consider the recoil pressure. Nevertheless, a high degree of linearity was observed across all the materials, confirming that these discrepancies are systematic rather than random, which supports the model's suitability for preliminary trend analysis.
- Outside the conduction melting mode, the model should primarily be used for trend analysis rather than absolute predictions, since it does not account for the physical mechanisms governing the keyhole and lack-of-fusion regimes.
- Dual-wavelength thermal camera measurements proved to be highly effective for validating the melt pool geometry simulations. Comparisons between the metallography and temperature measurements showed a discrepancy of only 6–9%, thus demonstrating the camera's performance as a process monitoring tool.

In summary, this work establishes a comprehensive methodology for the reliability assessment of LPBF thermal conductivity-based melt pool models. By utilizing simplified melt pool simulations validated in the present work, the computational and experimental costs associated with mapping the process windows for high-performance metallic alloys in LPBF can be significantly reduced.

Author Contributions: M.D.A.S.—performed the experiments, developed the image analysis code, carried out data analysis, prepared figures, and wrote the main manuscript; D.C.—participated in experimental work, contributed to code development, and reviewed the manuscript; A.L.—performed numerical simulations and contributed to manuscript writing; A.K.—supervised the work and reviewed the manuscript; V.B.—conceived the study, supervised the project, and reviewed the manuscript. All authors have read and agreed to the published version of the manuscript.

Funding: This research was funded by the Natural Sciences and Engineering Research Council of Canada (NSERC) under Discovery Grants RGPIN-2020-05800 (V. Brailovski) and RGPIN-2025-04142 (A. Kreitcberg).

Data Availability Statement: The datasets generated and analyzed during the current study, including experimental measurements and processed data, are available from the corresponding author upon reasonable request. Representative 3D models associated with this study are also available upon request. The code used for thermal image acquisition is not publicly available due to the inclusion of proprietary components but may be partially shared upon reasonable request, subject to restriction.

Acknowledgments: The authors acknowledge the financial support provided by NSERC (Natural Sciences and Engineering Research Council of Canada) under the Discovery Grant program. The authors also acknowledge the contributions of Emma Bisserié in sample preparation and analysis. During the preparation of this study, the authors used ChatGPT, gpt-4.0, for the purposes of debugging code and translating texts. The authors have reviewed and edited the output and take full responsibility for the content of this publication.

Conflicts of Interest: The authors declare no conflicts of interest.

Abbreviations

The following abbreviations are used in this manuscript:

LPBF	Laser powder bed fusion
HAZ	Heat affected zone
LED	Laser energy density
ROI	Region of interest
FE	Finite element
NDF	Neutral density filter
RMSE	Root mean square error
PSD	Particle size distribution
CBD	Coefficient of bulk powder density
LOF	Lack of fusion
CMOS	Complementary metal oxide semiconductor

Appendix A

Table A1. Simulated widths and associated relative errors according to metallographic observations.

	IN625			316L			CoCr		
	Exp. (µm)	**Model (µm)**	**Error (%)**	**Exp. (µm)**	**Model (µm)**	**Error (%)**	**Exp. (µm)**	**Model (µm)**	**Error (%)**
P0	139 ± 22	167	−20	134 ± 19	146	−9	155 ± 15	167	−7
P1	176 ± 17	217	−23	154 ± 20	167	−8	170 ± 22	187	−10
P2	166 ± 21	197	−19	140 ± 19	177	−26	166 ± 19	177	−6
P3	167 ± 31	167	0	142 ± 19	157	−11	156 ± 20	136	13
P4	138 ± 14	177	−28	129 ± 18	136	−5	173 ± 20	167	3
P5	141 ± 15	157	−11	136 ± 34	146	−8	170 ± 22	167	2
P6	128 ± 24	167	−30	129 ± 31	146	−13	167 ± 30	157	6
P7	120 ± 33	116	3	118 ± 29	116	2	148 ± 16	136	8
P8	133 ± 28	126	6	124 ± 31	126	−1	150 ± 20	136	9
P9	114 ± 27	126	−11	119 ± 27	106	11	114 ± 28	96	16

Table A2. Simulated lengths and associated relative errors according to camera observations.

	IN625			316L			CoCr		
	Camera (µm)	**Model (µm)**	**Error (%)**	**Camera (µm)**	**Model (µm)**	**Error (%)**	**Camera (µm)**	**Model (µm)**	**Error (%)**
P0	305 ± 44	309	−1	326 ± 51	333	−2	347 ± 51	364	−5
P1	328 ± 60	333	−2	315 ± 58	291	8	318 ± 49	327	−3
P2	286 ± 43	291	−2	386 ± 56	376	3	346 ± 55	345	0
P3	236 ± 32	230	3	361 ± 54	358	1	179 ± 38	170	5
P4	343 ± 65	364	−6	252 ± 57	242	4	307 ± 41	297	3
P5	229 ± 31	230	−1	380 ± 43	406	−6	382 ± 52	376	2
P6	329 ± 100	333	−1	388 ± 47	382	2	345 ± 49	358	−4
P7	162 ± 36	158	2	260 ± 55	255	2	270 ± 47	285	−5
P8	205 ± 65	218	−6	323 ± 53	315	3	340 ± 54	370	−8
P9	238 ± 76	236	1	309 ± 63	315	−2	194 ± 33	200	−3

Table A3. Simulated depths and associated relative errors according to metallographic observations.

	IN625			316L			CoCr		
	Exp. (µm)	**Model (µm)**	**Error (%)**	**Exp. (µm)**	**Model (µm)**	**Error (%)**	**Exp. (µm)**	**Model (µm)**	**Error (%)**
P0	92 ± 6	73	20	55 ± 9	64	−16	114 ± 20	76	33
P1	201 ± 14	103	49	110 ± 6	79	28	146 ± 28	82	44
P2	158 ± 16	91	42	118 ± 7	79	33	147 ± 26	85	42
P3	118 ± 29	73	38	68 ± 7	73	−7	64 ± 14	64	0
P4	142 ± 18	82	42	26 ± 6	61	−134	97 ± 22	76	22
P5	80 ± 14	70	13	52 ± 5	64	−22	131 ± 43	76	42
P6	121 ± 14	70	42	60 ± 4	64	−6	107 ± 36	70	35
P7	11 ± 3	48	−327	21 ± 14	52	−149	57 ± 24	61	−8
P8	33 ± 5	52	−59	22 ± 8	52	−137	70 ± 31	64	9
P9	46 ± 7	52	−14	18 ± 9	45	−145	34 ± 13	42	−24

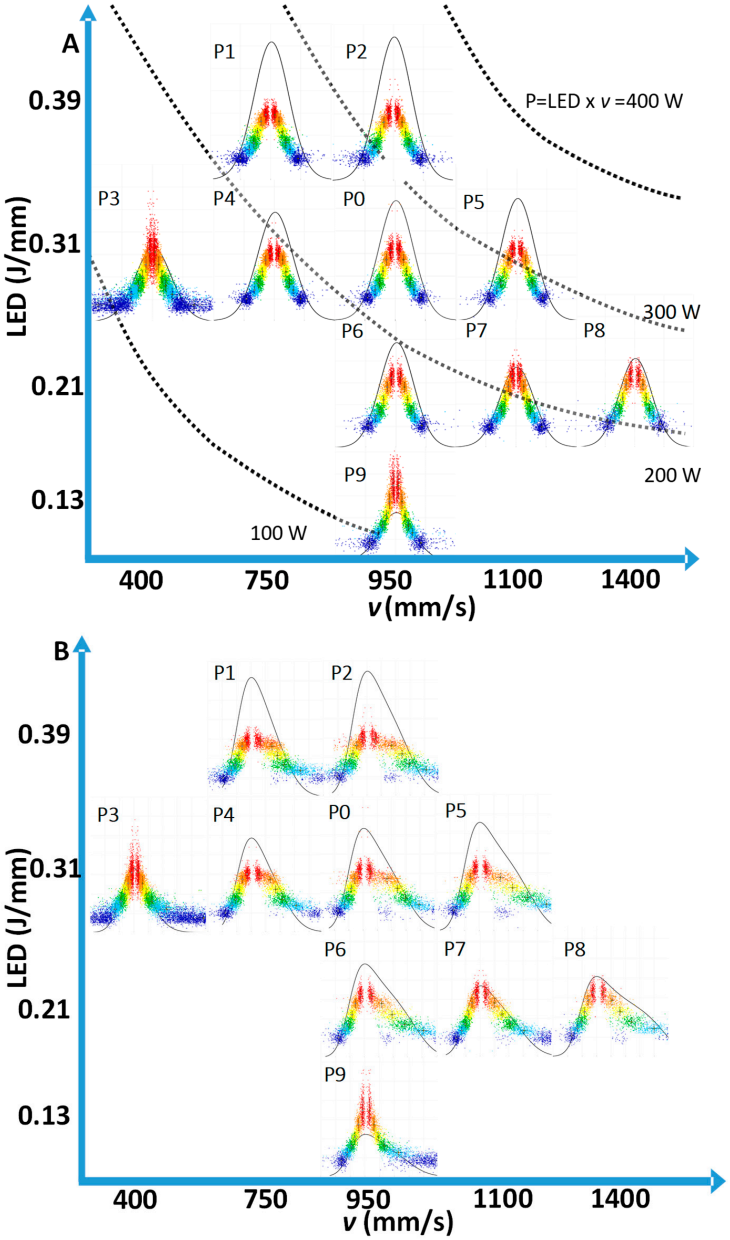


Figure A1. CoCr melt pool temperature profiles obtained using simulations (black lines) and camera observations (point clouds): (**A**) width, (**B**) length. Each color in the point clouds corresponds to one of the intensity isoline levels (5, 10, 30, 50, 70, and 90% of the peak λ_1 intensity).

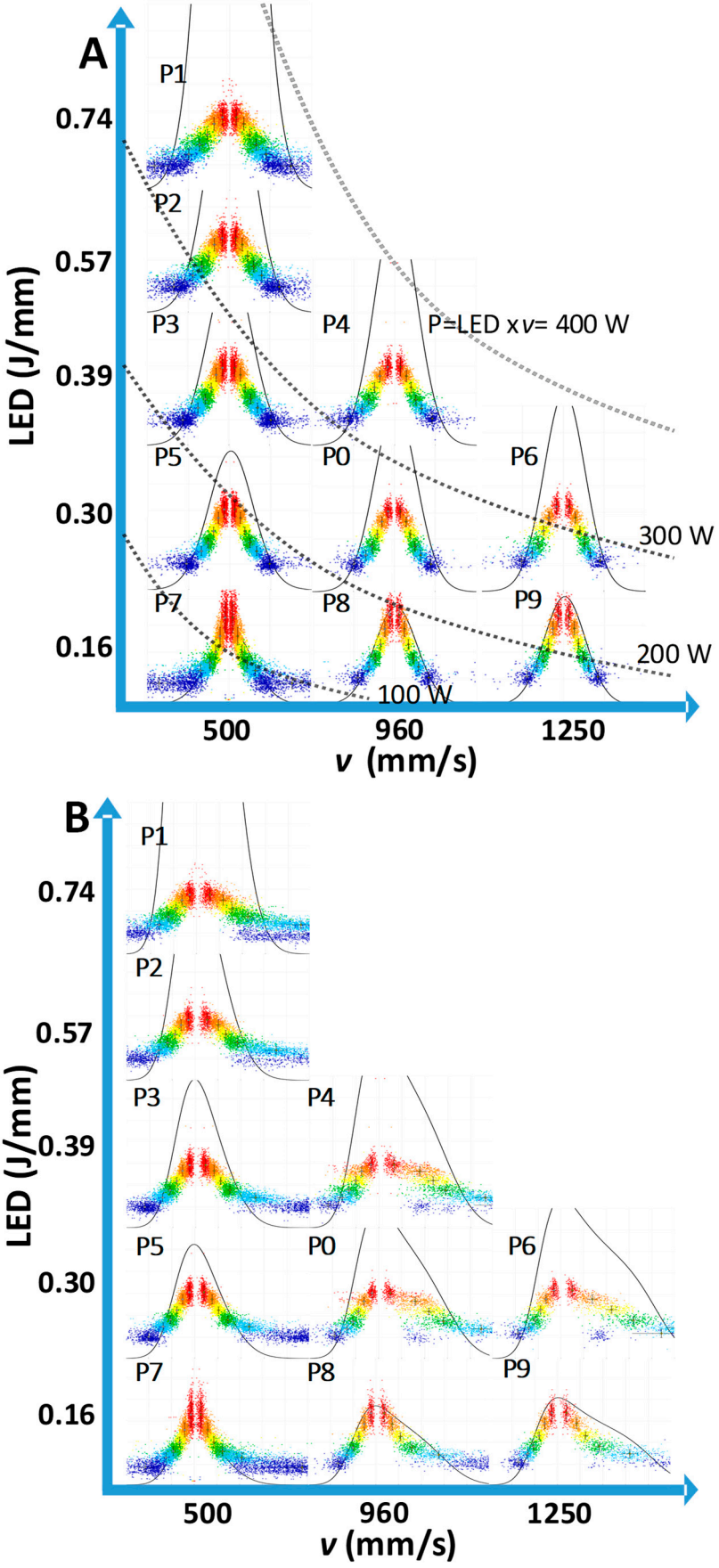


Figure A2. IN625 melt pool temperature profiles obtained using simulations (black lines) and camera observations (point clouds): (**A**) width, (**B**) length. Each color in the point clouds corresponds to one of the intensity isoline levels (5, 10, 30, 50, 70, and 90% of the peak λ_1 intensity).

References

1. Wang, J.; Zhu, R.; Liu, Y.; Zhang, L. Understanding Melt Pool Characteristics in Laser Powder Bed Fusion: An Overview of Single- and Multi-Track Melt Pools for Process Optimization. *Adv. Powder Mater.* **2023**, *2*, 100137. [CrossRef]
2. Khairallah, S.A.; Anderson, A.T.; Rubenchik, A.; King, W.E. Laser Powder-Bed Fusion Additive Manufacturing: Physics of Complex Melt Flow and Formation Mechanisms of Pores, Spatter, and Denudation Zones. *Acta Mater.* **2016**, *108*, 36–45. [CrossRef]
3. Carter, L.N.; Martin, C.; Withers, P.J.; Attallah, M.M. The Influence of the Laser Scan Strategy on Grain Structure and Cracking Behaviour in SLM Powder-Bed Fabricated Nickel Superalloy. *J. Alloys Compd.* **2014**, *615*, 338–347. [CrossRef]
4. Shrestha, S.; Chou, K. Formation of Keyhole and Lack of Fusion Pores during the Laser Powder Bed Fusion Process. *Manuf. Lett.* **2022**, *32*, 19–23. [CrossRef]
5. Yang, X.; Li, Y.; Li, B. Formation Mechanisms of Lack of Fusion and Keyhole-Induced Pore Defects in Laser Powder Bed Fusion Process: A Numerical Study. *Int. J. Therm. Sci.* **2023**, *188*, 108221. [CrossRef]
6. Wang, R.; Garcia, D.; Kamath, R.R.; Dou, C.; Ma, X.; Shen, B.; Choo, H.; Fezzaa, K.; Yu, H.Z.; Kong, Z. In Situ Melt Pool Measurements for Laser Powder Bed Fusion Using Multi Sensing and Correlation Analysis. *Sci. Rep.* **2022**, *12*, 13716. [CrossRef]
7. Chen, S.; Yang, Y.; Liu, S.; Duan, M. In-Situ Additive Manufacturing Deposition Trajectory Monitoring and Compensation with Thermal Camera. *Addit. Manuf.* **2023**, *78*, 103820. [CrossRef]
8. Mitrašinović, A.; Đurđević, T.; Nešković, J.; Radosavljević, M. Temperature Monitoring in Metal Additive Manufacturing in the Era of Industry 4.0. *Technologies* **2025**, *13*, 317. [CrossRef]
9. Shrestha, S.; Chou, K. Single Track Scanning Experiment in Laser Powder Bed Fusion Process. *Procedia Manuf.* **2018**, *26*, 857–864. [CrossRef]
10. Leclercq, A.; Brailovski, V. Improving Laser Powder Bed Fusion Printability of Tungsten Powders Using Simulation-Driven Process Optimization Algorithms. *Materials* **2024**, *17*, 1865. [CrossRef]
11. Letenneur, M.; Kreitcberg, A.; Brailovski, V. Optimization of Laser Powder Bed Fusion Processing Using a Combination of Melt Pool Modeling and Design of Experiment Approaches: Density Control. *JMMP* **2019**, *3*, 21. [CrossRef]
12. Schuöcker, D. *Handbook of the EuroLaser Academy, Volume 2*; Chapman & Hall: London, UK; Weinheim, Germany, 1998.
13. Sumin Sih, S.; Barlow, J.W. The Prediction of the Emissivity and Thermal Conductivity of Powder Beds. *Part. Sci. Technol.* **2004**, *22*, 291–304. [CrossRef]
14. Bala, K.; Pradhan, P.R.; Saxena, N.S.; Saksena, M.P. Effective Thermal Conductivity of Copper Powders. *J. Phys. D Appl. Phys.* **1989**, *22*, 1068–1072. [CrossRef]
15. Tolias, P. Analytical Expressions for Thermophysical Properties of Solid and Liquid Tungsten Relevant for Fusion Applications. *Nucl. Mater. Energy* **2017**, *13*, 42–57. [CrossRef]
16. Ashby, A.; Guss, G.; Ganeriwala, R.K.; Martin, A.A.; DePond, P.J.; Deane, D.J.; Matthews, M.J.; Druzgalski, C.L. Thermal History and High-Speed Optical Imaging of Overhang Structures during Laser Powder Bed Fusion: A Computational and Experimental Analysis. *Addit. Manuf.* **2022**, *53*, 102669. [CrossRef]
17. Mahmoudi, M.; Tapia, G.; Karayagiz, K.; Franco, B.; Ma, J.; Arroyave, R.; Karaman, I.; Elwany, A. Multivariate Calibration and Experimental Validation of a 3D Finite Element Thermal Model for Laser Powder Bed Fusion Metal Additive Manufacturing. *Integr. Mater. Manuf. Innov.* **2018**, *7*, 116–135. [CrossRef]
18. Goossens, L.R.; Van Hooreweder, B. A Virtual Sensing Approach for Monitoring Melt-Pool Dimensions Using High Speed Coaxial Imaging during Laser Powder Bed Fusion of Metals. *Addit. Manuf.* **2021**, *40*, 101923. [CrossRef]
19. Park, H.; Mullin, K.M.; Kumar, V.; Wander, O.; Pollock, T.M.; Zhu, Y. Resolving Thermal Gradients and Solidification Velocities during Laser Melting of a Refractory Alloy. *Addit. Manuf.* **2025**, *105*, 104750. [CrossRef]
20. Leclercq, A.; Mouret, T.; Brailovski, V. Laser Powder Bed Fusion of Molybdenum: Density, Structure and Mechanical Properties at Room and Elevated Temperatures. *Mater. Sci. Eng. A* **2025**, *929*, 148004. [CrossRef]
21. Hügel, H.; Dausinger, F. Interaction Phenomena. In *Handbook of the EuroLaser Academy*; Springer: New York, NY, USA, 1998; Volume 2, pp. 1–102.
22. Kang, S.H.; Jin, H.-H.; Jang, J.; Choi, Y.S.; Oh, K.H.; Foley, D.C.; Zhang, X. A Quantitative Evaluation of Microstructure by Electron Back-Scattered Diffraction Pattern Quality Variations. *Microsc. Microanal.* **2013**, *19*, 83–88. [CrossRef]
23. Gurrala, A.K.; Rahul, G.; Amalan, S.; Preejith, S.; Sivaprakasam, M. Eliminating Vertical Fixed Pattern Noise in CMOS-Based Endoscopic Images Using Modified Dark Frame Subtraction. In *Proceedings of the 2023 IEEE International Symposium on Medical Measurements and Applications (MeMeA), Jeju, Republic of Korea, 14–16 June 2023*; IEEE: Piscataway, NJ, USA, 2023; pp. 1–6.
24. Mitchell, J.A.; Ivanoff, T.A.; Dagel, D.; Madison, J.D.; Jared, B. Linking Pyrometry to Porosity in Additively Manufactured Metals. *Addit. Manuf.* **2020**, *31*, 100946. [CrossRef]
25. Wang, L.; Felicelli, S.D.; Craig, J.E. Experimental and Numerical Study of the LENS Rapid Fabrication Process. *J. Manuf. Sci. Eng.* **2009**, *131*, 041019. [CrossRef]
26. Kou, S. *Welding Metallurgy*, 1st ed.; Wiley: Hoboken, NJ, USA, 2002.

27. Sherby, O.D.; Burke, P.M. Mechanical Behavior of Crystalline Solids at Elevated Temperature. *Prog. Mater. Sci.* **1968**, *13*, 323–390. [CrossRef]
28. De Izarra, C.; Gitton, J.-M. Calibration and Temperature Profile of a Tungsten Filament Lamp. *Eur. J. Phys.* **2010**, *31*, 933–942. [CrossRef]
29. Myers, A.J.; Gobert, C.; Beuth, J.L.; Malen, J.A. High-Speed Imaging Investigation and Process Mapping of the Plume Behavior in Laser Powder Bed Fusion. *Addit. Manuf.* **2025**, *106*, 104797. [CrossRef]
30. Hooper, P.A. Melt Pool Temperature and Cooling Rates in Laser Powder Bed Fusion. *Addit. Manuf.* **2018**, *22*, 548–559. [CrossRef]
31. Myers, A.J.; Quirarte, G.; Ogoke, F.; Lane, B.M.; Uddin, S.Z.; Farimani, A.B.; Beuth, J.L.; Malen, J.A. High-Resolution Melt Pool Thermal Imaging for Metals Additive Manufacturing Using the Two-Color Method with a Color Camera. *Addit. Manuf.* **2023**, *73*, 103663. [CrossRef]
32. Soares, M.; Campion, D.; Kreitcberg, A.; Brailovski, V. In-Situ LPBF Monitoring Using a Dual-Wavelength Thermal Camera Calibrated via Ex-Situ Single-Track Measurements. Available online: https://ssrn.com/abstract=6437579 (accessed on 18 March 2026).
33. Yang, Z.; Zhang, S.; Ji, X.; Liang, S.Y. Model-Based Sensitivity Analysis of the Temperature in Laser Powder Bed Fusion. *Materials* **2024**, *17*, 2565. [CrossRef]
34. De Leon, E.; Riensche, A.; Bevans, B.D.; Billings, C.; Siddique, Z.; Liu, Y. A Review of Modeling, Simulation, and Process Qualification of Additively Manufactured Metal Components via the Laser Powder Bed Fusion Method. *JMMP* **2025**, *9*, 22. [CrossRef]
35. Karayagiz, K.; Elwany, A.; Tapia, G.; Franco, B.; Johnson, L.; Ma, J.; Karaman, I.; Arróyave, R. Numerical and Experimental Analysis of Heat Distribution in the Laser Powder Bed Fusion of Ti-6Al-4V. *IISE Trans.* **2019**, *51*, 136–152. [CrossRef]
36. Wang, W.; Ning, J.; Garmestani, H.; Liang, S.Y. Analytical Prediction of Molten Pool Dimensions in Powder Bed Fusion Considering Process Conditions-Dependent Laser Absorptivity. *Appl. Sci.* **2022**, *12*, 11926. [CrossRef]
37. Mao, Y.; Lin, X.; Zhu, H.; Zhu, K. Physics-Guided Spatiotemporal Approach for Melt Pool Size Prediction in Laser Powder Bed Fusion. *Virtual Phys. Prototyp.* **2024**, *19*, e2427243. [CrossRef]
38. Yang, Y.; Großmann, A.; Kühn, P.; Mölleney, J.; Kropholler, L.; Mittelstedt, C.; Xu, B.-X. Validated Dimensionless Scaling Law for Melt Pool Width in Laser Powder Bed Fusion. *J. Mater. Process. Technol.* **2022**, *299*, 117316. [CrossRef]
39. Liu, S.; Li, R.; Zhou, J.; Dai, C.; Yu, J.; Zhang, Q. Physics-Based Data Augmentation Enables Accurate Machine Learning Prediction of Melt Pool Geometry. *Appl. Sci.* **2025**, *15*, 8587. [CrossRef]
40. Zhang, Z.; Zhang, T.; Sun, C.; Karna, S.; Yuan, L. Understanding Melt Pool Behavior of 316L Stainless Steel in Laser Powder Bed Fusion Additive Manufacturing. *Micromachines* **2024**, *15*, 170. [CrossRef]
41. Cox, B.; Ghayoor, M.; Doyle, R.P.; Pasebani, S.; Gess, J. Numerical Model of Heat Transfer during Laser Powder Bed Fusion of 316L Stainless Steel. *Int. J. Adv. Manuf. Technol.* **2022**, *119*, 5715–5725. [CrossRef]
42. Guo, K.; Ji, Y.; Li, Y.; Kang, X.; Bai, H.; Ren, H. Numerical Simulation of Temperature Field and Melt Pool Characteristics of CP-Ti Manufactured by Laser Powder Bed Fusion. *Metals* **2022**, *13*, 11. [CrossRef]
43. Holla, V.; Grünewald, J.; Kopp, P.; Praegla, P.M.; Meier, C.; Wudy, K.; Kollmannsberger, S. Validity of Thermal Simulation Models for Different Laser Beam Shapes in Bead-on-Plate Melting. *Integr. Mater. Manuf. Innov.* **2024**, *13*, 969–985. [CrossRef]
44. Zhao, C.; Parab, N.D.; Li, X.; Fezzaa, K.; Tan, W.; Rollett, A.D.; Sun, T. Critical Instability at Moving Keyhole Tip Generates Porosity in Laser Melting. *Science* **2020**, *370*, 1080–1086. [CrossRef]
45. Huang, Y.; Fleming, T.G.; Clark, S.J.; Marussi, S.; Fezzaa, K.; Thiyagalingam, J.; Leung, C.L.A.; Lee, P.D. Keyhole Fluctuation and Pore Formation Mechanisms during Laser Powder Bed Fusion Additive Manufacturing. *Nat. Commun.* **2022**, *13*, 1170. [CrossRef]

Disclaimer/Publisher's Note: The statements, opinions and data contained in all publications are solely those of the individual author(s) and contributor(s) and not of MDPI and/or the editor(s). MDPI and/or the editor(s) disclaim responsibility for any injury to people or property resulting from any ideas, methods, instructions or products referred to in the content.